Temperature Dependent Qualities of Amorphous Silicon and Amorphous Silicon Carbide Passivating Stacks

by

Alec James Jackson

A Thesis Presented in Partial Fulfillment
of the Requirements for the Degree
Master of Science

Approved June 2016 by the
Graduate Supervisory Committee:

Zachary Holman, Chair
Mariana Bertoni
Michael Kozicki

ARIZONA STATE UNIVERSITY

August 2016

ABSTRACT

Layers of intrinsic hydrogenated amorphous silicon and amorphous silicon carbide were prepared on a polished, intrinsic crystalline silicon substrate via plasma-enhanced chemical vapor deposition to simulate heterojunction device relevant stacks of various materials. The minority carrier lifetime, optical band gap and FTIR spectra were observed at incremental stages of thermal annealing. By observing the changes in the lifetimes the sample structure responsible for the most thermally robust surface passivation could be determined. These results were correlated to the optical band gap and the position and relative area of peaks in the FTIR spectra related to to silicon-hydrogen bonds in the layers. It was found that due to an increased presence of hydrogen bonded to silicon at voids within the passivating layer, hydrogenated amorphous silicon carbide at the interface of the substrate coupled with a hydrogenated amorphous silicon top layer provides better passivation after high temperature annealing than other device structures.

DEDICATION

To my parents, for instilling in me a joy for the pursuit of knowledge and supporting me throughout my endeavors.

ACKNOWLEDGMENTS

First and foremost I'd like to acknowledge the tireless work of my advisor Zachary Holman. Without Zak, I would not have attended ASU nor have had the opportunity to be contributor in an excellent group. I'm beyond grateful for the chance to work under such a brilliant mind and gain the experience I needed to succeed in a research setting. I'd also like to acknowledge Mathieu Boccard, who created the framework for this study and guided me through the entire process. His earlier work made this study possible, and I hope this thesis provides a fraction of his guidance for future students.

TABLE OF CONTENTS

Page

LIST OF FIGURES vi

CHAPTER

1 PASSIVATION IN SILICON HETEROJUNCTION SOLAR CELLS ... 1

1.1 HIT Solar Cell Structure 2

1.2 Amorphous Silicon Carbide 4

2 EXPERIMENTAL PROCEDURE 6

2.1 Sample Fabrication 6

2.2 Characterization Techniques 7

2.2.1 Annealing 8

2.2.2 Measuring Carrier Lifetime 9

2.2.2.1 Photoconductance Decay 9

2.2.2.2 Data Collection 11

2.2.3 Band Gap Determination 12

2.2.3.1 Ellipsometry 12

2.2.3.2 Data Collection 14

2.2.4 Hydrogen Bonds 16

2.2.4.1 FTIR Spectroscopy 17

2.2.4.2 FTIR Spectra Collection 20

3 DATA ANALYSIS 25

3.1 Fitting IR Spectra in *Origin* 25

4 RESULTS AND DISCUSSION 29

4.1 Lifetime 30

4.2 Band gap 32

CHAPTER Page

4.3 FTIR Spectroscopy 36

4.4 Conclusion 41

REFERENCES 43

LIST OF FIGURES

Figure Page

1 A Schematic Detailing the Cross-Sectional Structure of the Experimental Samples 7

2 An Example of the Experimental Ellipsometric Data and a Fitting Model ... 15

3 A Screenshot of the Monitor Function in the Perkin-Elmer FTIR Data Collection Software 21

4 A Screenshot of the Main Screen of the FTIR Data Collection Software 24

5 A Graph of the Minority Carrier Lifetimes as a Function of Annealing Temperature 29

6 A Plot of the Optical Band Gap of the Sample Layers as a Function of Annealing Temperature 33

7 A Plot of the Mean Square Error between the Curves Provide by the Ellipsometric Model and the Experimental Data 34

8 A Graph Detailing the Collected Spectra for All Experimental Samples following Annealing 35

9 A Plot of the Total Area of the Curves Fitting the FTIR Peaks Related to Si-H Low and High Stretching Modes in A-SiC$_x$:H 38

10 Plots of the Position and Area of the Fitted Curves for the Si-H LSM and HSM FTIR Peaks 39

Chapter 1

PASSIVATION IN SILICON HETEROJUNCTION SOLAR CELLS

The demand for sources of alternative energy beyond fossil fuels combined with the relative abundance of silicon has historically driven the market for silicon-based photovoltaics. These solar cells rely on the semiconductor nature of silicon, which enables the generation of electron-hole pairs through exposure to incident radiation. Typical device structures rely on diffused junctions to create charge separation and generate electrical current. These junctions are formed by diffusing or implanting dopants into a crystalline silicon (c-Si) substrate, to promote bending of the valence and conduction bands and enable electron-hole separation. The carriers are transported through the c-Si bulk via drift and diffusion. This current is collected at the interface, generally though the use of an ohmic metal contact. The presence of defects at the bulk interface, such as lattice mismatch or dangling bonds, results in carrier recombination. These recombination sites lead to increased surface recombination velocities, which describe the rate at which carriers move towards the surface. High surface recombination velocities decrease the minority carrier density, leading to a drop in open-circuit voltage and overall cell efficiency. While high surface recombination velocities can be mitigated by reducing defects and introducing a back surface field, the efficiency of c-Si diffuse junction cells is inherently limited. While many solar cell manufacturers are looking beyond silicon-based technologies, such as III-IV materials and other thin-film photovoltaics, others have opted to continue working with silicon outside of the classic diffused junction structure.

1.1 HIT Solar Cell Structure

A common replacement for the diffuse junction structure is an amorphous silicon/crystalline silicon heterojunction, in which a doped amorphous silicon (a-Si) layer is deposited on a c-Si wafer. An oppositely doped a-Si layer is deposited on the backside of the substrate, creating band bending within the substrate to promote charge separation and ultimately create an electrical current that is collected by metal contacts on the surface of the amorphous layers.. Unlike a diffused junction cell in which the location of the junction is determined by the gradient of embedded dopants within the bulk, an HIT cell junction has no physically defined location in the substrate. A heterojunction structure has several distinct advantages over the classic diffused junction. The symmetrical structure cuts down on unique processing steps. Furthermore, the introduction of wide bandgap amorphous layers displaces the highly-recombination active sites in the contact metal away from the wafer surfaces, and when intrinsic these films can reduce the c-Si surface state density [1]. This *passivation* reduces the effects of surface recombination sites and helps increase carrier lifetime in the device, leading to larger voltages and increased cell efficiency. These benefits makes the heterojunction structure a great candidate for high-efficiency silicon solar cells, and initial research on its viability began as early as 1990 [2].

The significant upside of heterojunction structure is the quality of the interface between the amorphous and crystalline silicon, which exhibit fewer surface recombination sites than the interfaces in classic diffuse junction cells. The surface recombination sites may be attributed to dangling bands at the film/substrate interface, which offer electrically favorable states for free carriers. The free carriers are more likely to recombine at the dangling bonds, decreasing the population of minority carriers.

By limiting the population of electrons in the valence and conduction band, surface recombination sites decrease the quasi-Fermi-level separation and ultimately decrease the voltage across the device. One solution to this problem is the introduction of hydrogen within the amorphous layer, which acts to complete the dangling bonds and provide chemical passivation of the surface [3]. An abrupt heterojunction structure, in which the doped amorphous film is deposited directly on the crystalline substrate, creates a built in electrical field which acts to repel electrons or holes from surface states. This effect, known as electrical passivation, should lead to a further decrease in surface recombination at the interface. However, doped a-Si films have been experimentally shown to provide inferior passivation than their intrinsic counterparts [4]. Thus, the introduction of an intrinsic a-Si:H layer between the c-Si substrate and the doped a-Si film is necessary to effectively reduce recombination sites and obtain reasonable cell efficiency. This heterojunction with intrinsic thin layer (HIT) structure has recently been pursued as a viable option for a high-efficiency, silicon-based alternative to standard diffuse junction solar cells.

In 2014, Taguchi et. al set a record efficiency for an HIT solar cell on a thin silicon substrate at 24.7%, accomplished with the use of a p-type a-Si deposited on the front of a textured n-type c-Si substrate, and an n-type a-Si layer on the rear to create a back surface field structure [5], with a thin intrinsic a-Si:H passivating layer between the substrate and the doped films. The use of an intrinsic a-Si:H passivating layer has several limitations. Parasitic absorption of blue light by the a-Si:H layers at the front surface contributes to a loss of efficiency [6]. Furthermore, the passivation provided by a-Si:H undergoes degradation at high temperatures, limiting post-deposition processing steps to temperatures below 250 °C. This degradation is especially apparent for stacks of p-type and intrinsic a-Si layers. It has been posited

that this is an effect of the Fermi level in the intrinsic layer shifting towards the valence band due to the presence of the p-type layer, decreasing the energy required for defect creation due to bond breaking in this layer [7]. Thus, improving the temperature stability of the chemical passivation in an HIT structure will require modification of the intrinsic layer, as any p-type layer used for hole-collection will shift the Fermi level of the intrinsic layer. While it is generally not necessary to exceed temperatures of 250 °C when producing HIT cells, the inability to to incorporate high-temperature processes such as low-resistivity silver paste or silicon nitride anti-reflection coating hampers the progress of developing more efficient HIT cells. The implementation of a-Si in HIT structures as a bottom cell in a tandem device may also be inhibited by these temperature limitations, as the processes to fabricate most top cell candidates typically require temperatures above 400 °C [8]. In order to expand the utility of HIT solar cells, it will be important to overcome the shortcomings of intrinsic a-Si as a passivating layer and find a material better suited for high-temperature applications.

1.2 Amorphous Silicon Carbide

A promising replacement for a-Si passivating layers is amorphous hydrogenated silicon carbide. a-SiC:H has been shown to provide excellent passivation for doped crystalline substrates [9]. The carbon incorporation allows for adjustability of the optical bandgap over a wide range, reducing parasitic absorption. Furthermore, the incorporation of carbon to the a-Si:H matrix leads to an increase in hydrogen incorporation, decrease in the diffusion coefficient of hydrogen and an increase in the temperature of hydrogen effusion peaks [10]. These effects are linked to the stronger bonding of hydrogen to carbon than to silicon and would tend to lead to an increase

of the passivating qualities at high temperatures following a reduced formation of dangling bonds due to hydrogen effusion. While the increase in hydrogen incorporation would tend to lead to better passivation, the incorporation of carbon also leads to an increase in dangling bond density. Though intrinsic and n-type a-SiC:H films have been successfully demonstrated to passivate both n-type and p-type c-Si surfaces [11, 12, 13], the passivating qualities reported have yet to surpass those reached by intrinsic a-Si:H [14]. Studies on completed silicon heterojunction cells using n-type a-SiC:H emitters report moderate efficiencies of 18.5% in comparison to 21.4% reported for cells with a-Si:H emitters [16, 15]. However, such studies primarily investigate the utility of a-SiC:H as an emitter rather than an intrinsic passivating layer and did not investigate improved transparency or thermal stability.

This study expands upon previous investigations by Boccard and Holman on the passivation performance of various device-relevant stacks of a-SiC:H and a-Si:H following high-temperature annealing [17]. This study confirms that intrinsic a-SiC:H outperforms intrinsic a-Si:H as a passivating layer following exposure to high temperatures, especially when coupled with an intrinsic a-Si:H "capping" layer. These results correspond to the aforementioned study using doped a-Si:H emitters at the surface and an intrinsic a-SiC:H interface layer, suggesting the utility of extrapolating this analysis to HIT relevant structures. In order to explain the perceived differences in the passivating qualities of a-Si:H and a-SiC:H, ellipsometric and infrared spectroscopy measurements are used to track hydrogen content and bonding configurations within the passivating layers.

Chapter 2

EXPERIMENTAL PROCEDURE

In order to gain understanding about the type of bonds prevalent within the sample, as well as their effects on the passivating qualities of the layers, this study correlates Fourier transform infrared (FTIR) spectral data with photoconductance decay (PCD) lifetime measurements and ellipsometric band gap estimations.

2.1 Sample Fabrication

To gain understanding about the difference in passivating qualities of intrinsic a-SiC:H and a-Si:H, we need to compare the minority carrier lifetimes achieved with various device structures and investigate the hydrogen bonding and content within the films. As shown in Fig. 1, this study focused on four separate structures:

- **A**: 40-nm of a-Si
- **B**: 20-nm of a-SiC:H on top of 20-nm of a-Si:H
- **C**: 20-nm of a-Si:H on top of 20-nm of a-SiC:H
- **D**: 40-nm of a-SiC:H.

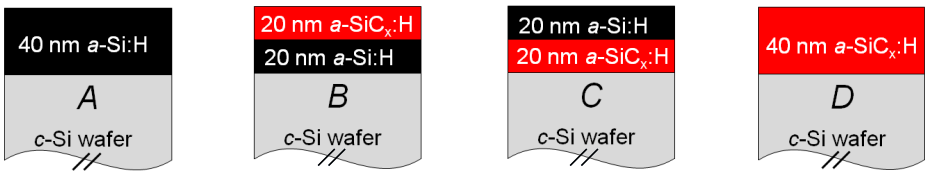

Figure 1. A schematic detailing the cross-sectional structure of the experimental samples

Note: All samples have the same total thickness and display vertically symmetric layers deposited on both sides of the substate.

The intrinsic a-SiC$_x$:H and a-Si:H films were deposited via plasma-enhanced chemical vapor deposition (PECVD) at a temperature of 250 °C and a pressure of 4.3 mbar from a mixture of silane, methane and hydrogen (SiH_4, CH_4, H_2). The methane flow ratio, R_{CH4}, is defined as the mass flow rate of CH_4 divided by the sum of SiH_4 and CH_4 mass flow rates and was set to 50% to achieve a-SiC:H and 0% for a-Si:H. Very little carbon was incorporated into the film, as secondary ion mass spectroscopy reveals that $R_{CH4=50\%}$ resulted in an atomic ratio of $\frac{C}{C+Si} = 4\%$ [17]. The flow of H_2 was kept steady at 400 sccm for all depositions. All samples were deposited on both sides of double-side-polished, n-type float zone c-Si wafers that were cleaned prior to deposition with piranha RCA-B.

2.2 Characterization Techniques

After fabrication, each sample was split into two parts. One piece was subjected to numerous annealing and characterization steps, while the other was saved for future analysis such as real-time FTIR and effusion measurements performed in *Anny*, a tool built for sample transfer between a glovebox and a vacuum analysis chamber outfitted with an IR transparent window and a sample heating element. A brief overview of the annealing and characterization procedure is as follows:

- Minority carrier lifetimes of the samples were determined by photoconductance decay measurements.
- The samples were measured via ellipsometry and the relevant optical properties such as band gap were determined by fitting the data to a model.
- FTIR spectral data of the samples was collected and compared to a reference "background" sample in order to isolate the signal from the amorphous stacks and determine the prevalence of hydrogen bonds within the passivating layers.
- The samples, as well as the FTIR reference "background" wafer, were annealed in a box furnace.
- The procedure was repeated in order to monitor the change in hydrogen content and lifetime with each successive annealing step.

Due to the cyclical nature of the experiment, it was important to maintain sample integrity throughout the process. Thus, the implementation of non-invasive measurement techniques enabled the same samples to be used throughout the process, increasing the consistency and accuracy of the results.

2.2.1 Annealing

The annealing was achieved in a box furnace, and the samples were subjected to ambient gasses and pressures. In the future, it may be pertinent to do the annealing in an inert gas or a vacuum to avoid the growth of oxide on the film surface, but for the purpose of this experiment the presence of oxygen within the film isn't of main concern. The temperature was set via a digital controller on the furnace, and sufficient time of about one hour was allowed to pass between changes in temperature in order to ensure consistency and accuracy. The samples were placed in the heated

furnace for 20 minutes, at which point they were removed and allowed to cool at room temperature and gasses before characterization. The initial annealing temperature was 200 °C, with each subsequent step 50 °C greater until reaching a final temperature of 500 °C.

2.2.2 Measuring Carrier Lifetime

A common method of characterizing the passivation provided by a film is to measure the minority carrier lifetime of the sample [18], or the amount of time it takes for a minority carrier to recombine. Longer minority carrier lifetimes indicate that the layer at the interface is indeed passivating, and comparing the lifetimes of different samples can provide information about which material is better suited for a passivating layer.

2.2.2.1 Photoconductance Decay

Under steady-state illumination, a semiconductor is in steady-state and a balance exists between the photogeneration and recombination of electron-hole pairs. Expressing this in terms of current densities yields

$$J_{\text{ph}} = J_{\text{rec}} \tag{2.1}$$

where the total recombination can be express in terms of the average excess carrier concentrations Δn_{av} and the sample thickness W and effective carrier lifetime τ_{eff} and elementary charge q

$$J_{\text{ph}} = J_{\text{rec}} = \frac{\Delta n_{\text{av}} q W}{\tau_{\text{eff}}}. \tag{2.2}$$

The excess carrier densities also results in a change in photoconductance, which can be expressed by

$$\Delta\sigma = qW\Delta n_{\text{av}} \left(\mu_{\text{n}} + \mu_{\text{p}}\right) \tag{2.3}$$

where μ_{n} and μ_{p} are the electron and hole mobilities respectively. Combining Eqs. 2.2 and 2.3 provides the effective carrier lifetime in terms of known or measurable quantities

$$\tau_{\text{eff}} = \frac{\Delta\sigma}{J_{\text{ph}} \left(\mu_{\text{n}} + \mu_{\text{p}}\right)}. \tag{2.4}$$

The photogenerated current density can be accurately estimated using the incident light intensity, and the conductance is measured via an inductive coupling coil. A more thorough investigation of the contactless measurement of photoconductance can be found in Yablonovitch and Gmitter [19], but the basic premise is that the induced voltage in a coil within a bridge circuit is coupled to the conductivity of the wafer. Thus for a sample with known mobilities, a measurement of the photoconductance and incident light intensity can provide an accurate measurement of the bulk minority carrier lifetime.

2.2.2.2 Data Collection

In this study, a Sinton lifetime tester using a contactless inductive coil provided a measurement of the minority carrier lifetime within the sample. The process does not require the use of ohmic contacts, so sample prep is minimal. A brief cleaning of the surface with a blast of nitrogen gas removes any particulates. Additionally, the sample must be large enough to completely cover the inductive coil for an accurate measurement of photoconductance. In this case, the measurements were conducted in "Transient" mode, in which the sample is briefly illuminated to generate electron hole pairs, and the change in conductance is measured after the illumination as the pairs recombine. The illumination source must be adjusted for this mode, and the duration of the illumination is set to 100 μs via the controls on the top of the lamp. The data is collected using a computer coupled to the Sinton tool, which the user interfaces with via an Excel spreadsheet. Within this spreadsheet, the illumination mode and carrier mobilities of the sample's bulk material is selected. The user can also specify the minority carrier density for which the lifetime should be reported. For this study, the lifetimes were reported for a minority carrier density of $1 \times 10^{15}\text{cm}^{-3}$. When the data is collected, a graph of the lifetime as a function of minority carrier density is displayed, which the user can review and adjust the settings as necessary. The spreadsheet also displays an error message if the measurement occurs during the illumination and provides an easy feedback system that suggest the necessary adjustments. The document automatically populates a secondary sheet with the collected data, and the whole document should be saved independently. These sheets are then imported via another Excel document, to extract only the relevant lifetime data for further graphical analysis.

2.2.3 Band Gap Determination

The structural adaptability of the amorphous silicon network allows the band gap to be widened by increasing the valence band offset through the introduction of hydrogen [20]. In general, the band gap is linearly dependent on the hydrogen content in the film, though it is suggested that the hydrogen bonding configuration plays a role in describing the slope of this behavior[21]. The band gap of a-SiC:H films is also tunable, and it has been shown that both the concentration and bonding configurations of carbon and hydrogen contribute to widening the band gap of intrinsic films [22]. The a-SiC:H band gap is non-linearly dependent on hydrogen and carbon content, suggesting that the type of Si-H and C-H bonds plays a prevalent role in band gap determination. However, the overall trend of increased hydrogen content widening the band gap holds true for both a-Si:H and a-SiC:H films. Using ellipsometry, one can measure the band gap of the individual layers within the passivating stacks and indirectly monitor the change in hydrogen content after successive annealing steps. This provides some information about the movement of hydrogen between the layers due to thermal diffusion and can help explain the observed differences in the passivating capabilities of the samples.

2.2.3.1 Ellipsometry

Ellipsometry is a contactless, non-invasive method of characterizing the optical properties of thin film dielectrics on semiconductor substrates [23]. It is essentially polarization spectrometry, as it measures the change in polarization of light upon reflection at the interface between a film and a substrate. Should the reader desire

deeper understanding, a much more exhaustive approach can be found in Tompkin's *Spectroscopic Ellipsometry and Reflectometry: A User's Guide* [24].

Ellipsometry relies on the transverse wave property of light, in which the oscillations in the electric and magnetic fields are perpendicular to the direction of propagation. The polarization of the light is defined by the orientation and the phase of the electric field vector. If the projected parallel and vertical components of this vector, ε_p and ε_s respectively, are orthogonal and in phase with each other then the light is linearly polarized. Elliptically polarized light results when the components have arbitrary phase and amplitude. The reflection coefficients,

$$R_p = \frac{\varepsilon_p\,(reflected)}{\varepsilon_p\,(incident)}; \qquad R_s = \frac{\varepsilon_s\,(reflected)}{\varepsilon_s\,(incident)} \tag{2.5}$$

describe the change in each component following reflection at a surface as a ratio of vector amplitudes and are not directly measurable. However, the complex reflection ratio ρ is measurable and can be described in terms of the ellipsometric angles Ψ and Δ

$$\rho = \frac{R_p}{R_s} = \tan(\Psi)\, e^{-i\Delta}. \tag{2.6}$$

The ellipsometric angles determine the changes in amplitude and phase that the parallel and perpendicular electric field components undergo upon reflection. By using Fresnel's and Cauchy equations in conjunction with regression analysis, it is possible to model the change in Ψ and ρ as a function of the wavelength of the incident light and extract the sample's optical parameters [18]. Many models take into account parameters such as sample thickness, index of refraction, extinction coefficient and optical band gap. While ellipsometry does not provide a direct measurement of these parameters, it offers a fast, contactless method of approximating the optical

characteristics of your sample. Though ellipsometry is a very powerful tool, it is a modeling technique that is inherently reliant on the known material parameters and is subject to inaccuracy. Results for film thickness or optical parameters should be verified by other techniques, such as a spectrometer or SEM measurements.

2.2.3.2 Data Collection

This study used a Woolam M2000 ellipstometry system and *CompletEASE* software package to collect and analyze the data. Preparing your sample for ellipsometry is minimal due to the contactless nature of the measurements. The sample can be cleaned using a blast of N_2 to remove any particulates, and is placed on a piece of paper on the sample stage. This paper helps avoid any interference due to the interface with the back of the sample and air.

CompletEASE offers an easy visual interface to ensure beam alignment, under the **Alignment** heading. By adjusting the micrometers on the sample stage and observing the subsequent changes in beam position, it is an easy process to achieve alignment with the collector. The location of the beam is digitally rendered as a red dot, and the collector location is displayed as an axis. A readout of the beam location in arbitrary units, with the origin being the collector, is also shown in the top left-hand corner of the display. In general, a reading of ± 1 or less for the x and y components is within acceptable range for measurements. The user then selects **Collect Data** and specifies the file location for the data to be saved. The ellipsometric angles are quickly measured and presented as a function of wavelength, which the user should review for any peculiarities. The user can then choose to analyze the spectra using a variety of models.

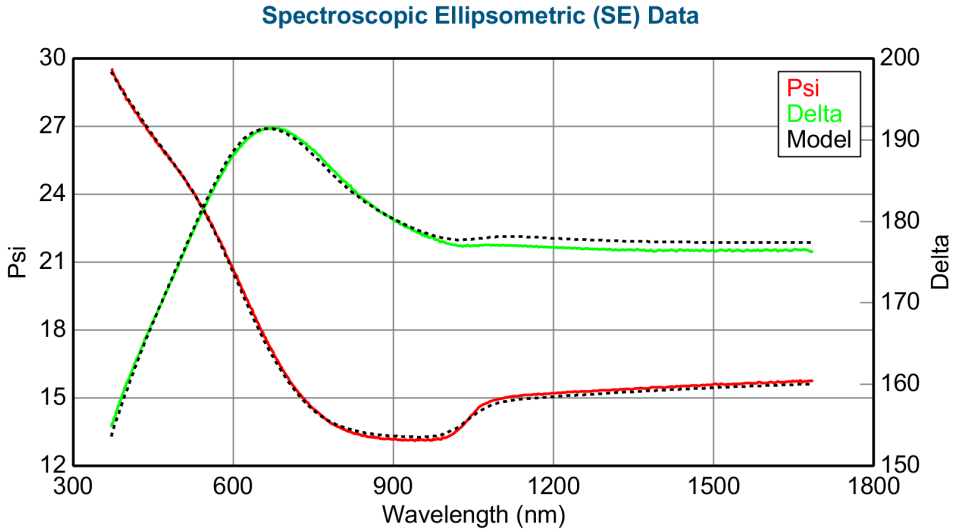

Figure 2. An example of the experimental ellipsometric data and a fitting model

In order to extract any relevant information, the spectra must be fit using a model. The user can select the material of the substrate, and import .mat files which specify models to describe the materials within the individual layers. A regression analysis is then executed, in which a specific oscillator model such as Tauc-Lorentz or Cody-Lorentz estimates the ellipsometric signal due to atomic transitions within the film. The Tauc-Lorentz oscillator model has been demonstrated to better fit amorphous semiconductor films than previous techniques, and has the advantage of containing optical band gap as a primary parameter [25]. Furthermore the Tauc-Lorentz technique has been demonstrated to accurately model the ellipsometric data of a-Si:H and a-SiC_x:H films [26].

In *CompletEase* the model parameters are automatically adjusted in an iterative approach to minimize the mean square error between the model and the experimental

data. The user can offer initial estimates of the various parameters so the analysis provides values that are near those which are expected. *CompletEASE* displays the collected ellipsometric angles Ψ and Δ as a function of wavelength with the model fit over-layed, as shown in Fig. 2. By hovering the cursor over a parameter and rolling the scroll-wheel, the user can manually change the values parameters and immediately observe it's effect on the fit in order to provide decent initial estimates. The user can also choose to "fix" certain parameters which they deem known or constant. In this study, a Tauc-Lorentz regression model was used in conjunction with previously established and verified material models for a-Si and a-SiC. The material models were developed using initial parameters from literature and their viability was tested by measuring samples with independently verified parameters. For the initial measurements of this study, the thickness parameter was allowed to vary with the other model parameters such as band gap and surface roughness. For the remainder of the measurements following the annealing steps, all of the parameters except the band gap were fixed at the initially estimated values. Thus, the variation in the band gap of the materials within the sample could be documented as a function of annealing temperature.

2.2.4 Hydrogen Bonds

The surface passivation provided by hydrogenated amorphous silicon and amorphous silicon carbide is dependent on both the hydrogen and carbon content and bonding within the interface film, and it has been demonstrated that a higher carbon content reduces hydrogen diffusion from the passivating layers [13]. In order to monitor the bonds present in the passivating layers, Fourier transform infrared spectroscopy,

or FTIR spectroscopy was utilized. FTIR spectroscopy is a contactless, non-invasive method of determining the presence and relative quantity of chemical bonds within a material via optical measurements [27]. This data was then correlated to the observed minority carrier lifetimes of each sample as a means of illuminating the perceived differences in passivating qualities of the various samples.

2.2.4.1 FTIR Spectroscopy

Spectroscopy is an optical technique of material characterization that relies on the unique transitions between quantized vibrational states of molecules. By energizing a molecule with an incident photon, the molecule exhibits a *vibrational mode* which involves approximately harmonic displacements of the atoms from their equilibrium position. These vibrations are anharmonic and can be described by a Morse type potential. The potential energy V is described by the equation

$$V_{iv} = h\nu_i \left(v_i + \frac{1}{2} \right) + h\nu_i x_i \left(v_i + \frac{1}{2} \right)^2 \tag{2.7}$$

where h is Planck's constant, ν_i is the fundamental frequency of the particular mode and v_i is the vibrational quantum number of the ith mode. The quantized nature of these vibrations lead to a discrete vibrational spectra comprised of the various vibrational modes found within a sample. The frequency of each mode is characterized by the functional group of atoms who exhibit large displacements and is minimally affected by other less mobile atoms within the bonding group. Thus, the observation of spectral features is often indicative of the specific chemical functional group within the lattice. Furthermore, each configuration has slightly different vibrational modes, resulting in a unique infrared spectrum for each type of bond. The uniqueness of

each spectra allows for the identification of the bonding configurations within a material simply through IR spectroscopy. However, the technique is not only limited to identification, it can also be used to quantify the bonding configurations present in a sample.

Beer's law is the fundamental law of quantitative spectroscopy. It relates the *absorbance* at a characteristic wavenumber to the concentration of that component in the sample. The *transmittance* of any sample at a wavenumber $\tilde{\nu}$ is given by the ratio of the radiant power leaving the rear surface of the sample $I(\tilde{\nu})$ to the power of the radiation at the front surface $I_0(\tilde{\nu})$. The transmittance is a function of sample thickness b and the linear absorption coefficient $\alpha(\tilde{\nu})$ and is given as

$$T(\tilde{\nu}) = \frac{I(\tilde{\nu})}{I_0(\tilde{\nu})} = \exp\left[-\alpha(\tilde{\nu})\, b\right] \tag{2.8}$$

and the absorbance is the base 10 logarithm of $1/T(\tilde{\nu})$

$$A(\tilde{\nu}) = \log_{10}\frac{1}{T(\tilde{\nu})} = \frac{1}{\ln 10}\alpha(\tilde{\nu})\, b. \tag{2.9}$$

The *absorptivity* is a function of wavenumber and is given by $a(\tilde{\nu}) = \frac{1}{\ln 10}\alpha(\tilde{\nu})$. If the sample is a mixture of N components, the absorbance of each component, i, at concentration c_i is described by

$$A_i(\tilde{\nu}) = a_i(\tilde{\nu})\, b c_i \tag{2.10}$$

and the total absorbance at that particular frequency is merely the sum of the components

$$A(\tilde{\nu}) = \sum_{i=1}^{N}\left[a_i(\tilde{\nu})\, b c_i\right]. \tag{2.11}$$

So, for any measurement of absorbance at known fundamental frequency of a vibrational mode, one can determine the relative concentration within the sample of the bonding configuration that relates to that particular mode. Using this method, it is possible to observe the change in hydrogen concentration and bond types within the passivating films as a function of annealing temperatures.

The apparatus used for FTIR spectroscopy is essentially an interferometer comprised of a radiation source, a beam splitter and a collector. The source provides a beam of collimated light in the IR range to the beam splitter, which splits this beam into two parts. One of the beams is incident on the sample and the reflected light undergoes a phase shift and variation in intensity. Upon recombination with the original beam, the signal is analyzed by the collector and an interferogram is produced in which the variation in intensity reflects the path difference between the two beams. In this case, the path difference is due to the reflection and absorption of the sample itself. However, the interferogram is a function of path difference, so the units of the abscissa are length. In order to apply Eqs. 2.8 and 2.10 to deduce the presence and concentration of chemical compounds within the sample, it is necessary to transform the interferogram to units of wavenumbers, or inverse length. This is accomplished through the use of a Fourier transform, which converts from a time domain to a frequency, or from a length to a wavenumber. For a sample that emits continuous radiation, rather than a single discrete spectral line, this process is not trivial and can only be accomplished through the use of a computer. Luckily, Perkin-Elmer provides software with their FTIR spectroscopy instrumentation which automatically performs this transform during data collection. A detailed explanation of using this software to perform accurate FTIR spectroscopic measurements will be covered in the following section.

2.2.4.2 FTIR Spectra Collection

The instrument used in this study was a Perkin-Elmer Frontier IR spectrometer, with data collection interfacing via the software *Spectrum*. The instrument was configured for diffuse reflectance infrared Fourier transform spectroscopy, or DRIFTS. This involved installing the diffuse reflectance attachment in place of the traditional transmission attachment. DRIFTS only collects the reflected light from the frontside of the sample, so the sample can be placed on a non-transparent platform or holder and measured, rather than having to be suspended in the beam path for transmission measurements. This accessory is primarily used for samples that result in a large amount of diffusion of the reflected light such as powders or textured wafers, as it utilizes a parabolic mirror to collect scattered light from the surface of the sample. It also allows for the use of a smaller sample than the transmission attachment, and makes it much easier to test the alignment of the signal beam. Finally, the DRIFTS accessory could be used in conjunction with a sealed analysis chamber with the sample in a controlled atmosphere and the measurements performed through an IR transparent window.

In order to ensure beam alignment with the DRIFTS accessory, a small mirror is placed in the sample holder. Then, the total energy of the reflected signal is measured in *Spectrum* by selecting the **Monitor** function under the **Process** tab in the toolbar at the top of the window. As shown in Fig. 3, this function displays the current measurement of the total energy collected by the detector, as well as the maximum value measured during the session. By adjusting the micrometer on the top of the DRIFTS accessory, the position of the parabolic mirror moves and the amplitude of the signal changes accordingly. In order to ensure the maximum signal, the sample

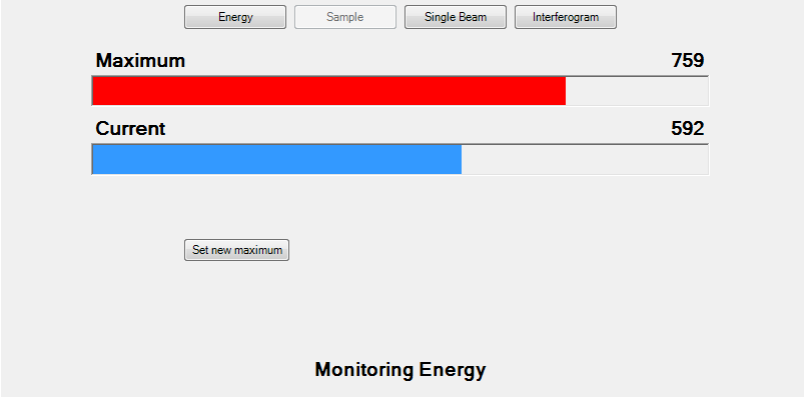

Figure 3. A screenshot of the Monitor function in the Perkin-Elmer FTIR data collection software

The "Maximum" reading displays the largest intensity light recorded at the collector during this session, while the "Current" reading shows the current reading. Proper sample and beam alignment is achieved when the "Current" reading is a maximum.

holder and mirror should be positioned such that the signal detected is of maximum energy. Once this is accomplished, the physical apparatus is properly aligned and the user can focus on configuring the data collection parameters.

The collection parameters are adjusted by selecting **Instrument** from the **Setup** panel on the right hand side of the screen. This opens a bar at the bottom of the spectral display window, and the tab **Setup Instrument Basic** is selected. Here, the user can set the range of the spectrum to be collected, the interval of collection, the resolution the number of scans and the abscissa and ordinate units. The most commonly used units for FTIR spectra is wavenumber and absorbance for abscissa and ordinate respectively. The range sets how much of the spectrum should be collected, and can be adjusted to focus on previously known spectral characteristics. The interval is merely how "wide" the steps between each adjacent data point is. Smaller intervals generally lead to more precise data, though the minimal detectable signal amplitude can also be a limiting factor to obtaining smooth data that lacks abrupt changes. The

resolution determines the size of spectral features that the software should display. Small resolution can pick out very fine features, but can also lead to very noisy data as the software is more likely to display any variation as a feature rather than an outlier. Larger resolution can lead to cleaner data but may result in finer features being ignored. The number of times the software scans through the full spectral range is set by the number of scans. Multiple scans leads to better, more accurate data, as outliers and statistical noise will be averaged out. However, each scan takes about 5 seconds so more scans means a longer measurement time. It is suggested that the experimenter run a few sample measurements to determine the optimum interval and resolution for the desired spectral characteristics. In order to minimized the time of measurements, the range should be adjusted to only include the spectral region of interest and the number of scans should be limited. However, the data collection process is relatively quick, so time should not be much of an issue unless in situ measurements are being performed. For this experiment, all data was collected over a range of 400 to 3200 cm^{-1}, with a resolution of 8 cm^{-1}, and interval of 2 cm^{-1} for a total of 100 scans.

After configuring the instrument, data collection begins. First, the user must take a "background" spectrum, which will be subtracted from the collected data. This corrects for any constant sources of signal, such as the presence of atmospheric gasses or a deposition substrate. In this case, we want to isolate the signal of the passivating layers from that due to the c-Si substrate. To accomplish this, we collect "background" data from a bare, double-side-polished c-SI wafer that matches the substrate used for the samples and *Spectrum* automatically subtracts this signal from any subsequent measurements. The "background" sample is placed onto the sample holder, and its position can be verified using the **Monitor** function as described above. To start a

"background" collection, **Background** is selected under the **Measurement** heading and the scans begin. After completion, the "background" is removed from the sample holder and a true sample is put in place. The "Sample ID" can be input, and will become the automatically applied filename for this sample as well as a description of the sample. Finally, the user clicks **Scan** in the toolbar or under the **Measurement** heading and the spectrum is collected.

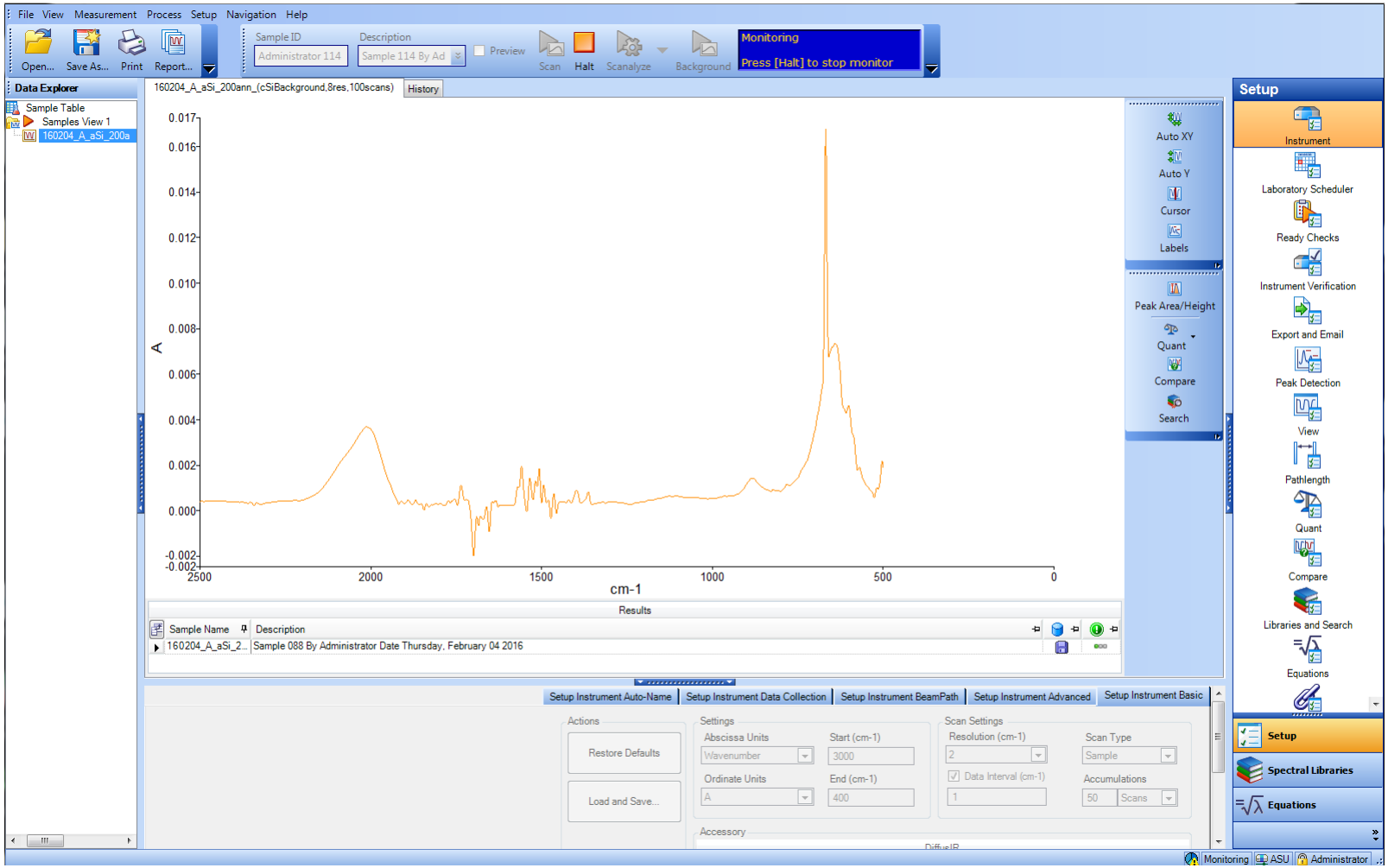

Figure 4. A screenshot of the main screen of the FTIR data collection software

Chapter 3

DATA ANALYSIS

While photoconductance decay and ellipsometry characterization require very little analysis in order to obtain the lifetime and band gap, the FTIR spectra must undergo extensive post-measurement analysis to acquire quantitative information about the hydrogen bonding within the samples. As previously discussed, the intensity of an FTIR spectroscopy signal at a specific wavenumber directly relates to the concentration of the responsible chemical compound within the sample. By analyzing the contributions of vibrational modes for compounds of interest, such as silicon-hydrogen bonds, we can gain understanding about the quantity of specific chemical groups within the sample. This requires fitting the peaks of the spectra that are attributed to hydrogen bonds and comparing the area under these curves. The following section will detail how to automate the curve-fitting process in *Origin* in order to accommodate multiple data sets.

3.1 Fitting IR Spectra in *Origin*

After collecting the spectra, the FTIR data can be exported as a .csv to allow for analysis and visualization in various programs. In this case Origin was used, primarily for its powerful curve-fitting capabilities. *Origin* uses customizable themes to allow for quick processing of multiple data sets. For example, the **Peaks and Baseline** section under the **Analysis** tab in the toolbar allows the user to find peaks in the data and fit curves to these peaks. *Origin* offers complete control over the fitting process, which

is accessed by selecting **Open Dialog...** and interacting with the resulting **Peak Analyzer** window. The following section offers a guide through creating a template for curve fitting using the a single data set and Fit Peaks [Pro] option, as selected by the radio button on the first page of the **Peak Analyzer**.

First, the data is baseline corrected, which levels the spectra and makes sure the featureless portions of the spectra are set to zero. This enables the comparison of the magnitude of peaks and area of the fitted curves between multiple measurements that may have been shifted in amplitude. Establishing the baseline can be controlled by selecting the **User Defined** option in the pulldown menu. Baseline correction is accomplished by selecting points on the spectra that are expected to be zero and then interpolating the line between them and subtracting that line from the spectra. *Origin* can do the point selection automatically, or the user can select them manually for every dataset. The best way to process a bunch of datasets quickly is by trimming the data to spectral region of interest, with the ends of the range at featureless points that are expected to be zero. Selecting **Enable Auto Find** and setting the **Number of Points to Find** to 2 will automatically establish the ends of the curve as your baseline values and allows the baseline process to be automated for multiple datasets. However, sometimes *Origin* will make a mistake and select an inappropriate value, skewing the baseline and forcing the corrected data to tilt away from the horizontal axis. Thus it may be important to review the final curves and make sure your corrected data is level. In the next page, the baseline is created via direct interpolation or fitting the selected values to a user-defined function. If the selected values are similar and the baseline is expected to be linear, direct interpolation works just fine. The baseline treatment is accomplished in the next window, and it is important to select the **Auto Subtract Baseline** option in order to enable batch curve processing.

After the data has been baseline corrected, the location of the peaks of interest is determined. In this case, we are interested in determining the presence and relative quantity of the low and high stretching modes of Si-H bonds in a-Si:H and a-SiC:H, located between 1980 and 2120 cm^{-1} [29, 28]. It is better to manually define the peak position, as the spectra may not display clearly defined peaks at the known locations of interest and *Origin* may fail to automatically detect them. By unselecting **Enable Auto Find** and selecting **Peaks Info...** the user can add a peak center location and height. As the fit will adjust these values to create a more accurate model, it is not important that the *Origin*al location or height be exactly accurate for each data set. With the data baseline corrected and the peaks of interest selected, it is now time to perform the fit. Selecting the **Fit Control** button will bring up a pop-up window that allows the user to define initial fit parameters and set bounds on the range of values that the fit can try. To ensure accurate fits for batch processing, it is important to constrain the peak centers to reasonable ranges, generally ±20 cm6−1 from the expected location. It may also be necessary to restrict the amplitude and full-width at half-max of each peak to non-negative values. The model is then tested by selecting **Fit** which will iterate the model until the fit converges, and the fit curves are immediately displayed on the data set for review. If the model seems accurate and the user is confident that the method can be replicated for other data sets, the fit process can be saved as a *theme* by expanding the via the button in the top corner of the **Peak Analyzer** window. This theme can be applied by selecting multiple data sets and performing **Batch Peak Analysis Using Theme** within the **Peaks and Baseline** menu in the **Analysis** tab. This will produce an output sheet with the relevant fit information for each data set, such as peak position and area under the curves, which can then be used for further analysis. It also reports the R^2

values for each fit, which is an estimate of how well the model fits the experimental data. A common threshold for a good fit is $R^2 \geq 0.95$ and anything less suggests an unacceptable model.

Chapter 4

RESULTS AND DISCUSSION

Characterizing the passivation due to the amorphous layers is accomplished by measuring the minority carrier lifetimes within the sample. The following results show that an a-SiC:H layer at the c-Si interface outperforms a-Si:H after annealing. The rest of this section attempts to explain the apparent differences in passivating qualities by tracking the change in hydrogen content and Si-H bonds via ellipsometry and FTIR.

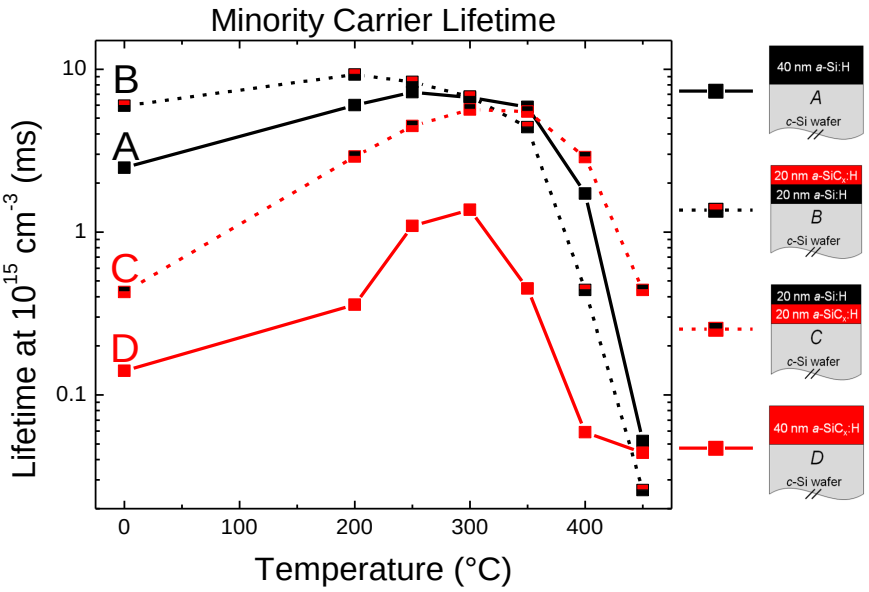

Figure 5. A graph of the minority carrier lifetimes as a function of annealing temperature

4.1 Lifetime

Figure 5 displays the measured lifetime of each sample as a function of the annealing temperature. The initial lifetimes following deposition and prior to any annealing are represented by the data points at a temperature of 0 °C, while the rest of the temperatures correspond directly to the setpoint temperature of the annealing furnace. The incorporation of carbon leads to an increase in the density of dangling bonds, leading to the relatively low initial lifetimes for structures with an a-SiC:H interface layer (samples C and D) in comparison to samples with an a-Si:H interface layer, A and B. Initially, there isn't enough hydrogen available at the interface to remove the increased number of dangling bonds. After exposure to higher temperatures, the lifetimes of all samples increases significantly. The change in passivation due to annealing is normally associated to hydrogen redistribution within the network [7] as free hydrogen diffuses through the layers and some of it removes the incomplete bonds at the lattice interface. This process appears to continue until temperatures reach about 300 °C, at which point Si-H bonds begin breaking and dangling bonds re-emerge, decreasing the lifetime. The perceived differences between the samples' rate of change in lifetime with respect to temperature may be explained by lower diffusion coefficient of hydrogen in a-SiC than a-Si. For the first two annealing steps, the lifetimes of A and B appear to increase at similar rates, while C increases more rapidly. In comparison, sample D experiences a drastic increase in lifetime after the first step. The samples with a-SiC interface layers appear to require more time and higher temperatures to allow hydrogen to diffuse to the interface. Furthermore, the a-Si:H may act as a "source" of hydrogen for a-SiC layers, as demonstrated by the lifetime discrepancy between samples C and D. The most compelling difference

between the samples is demonstrated at temperatures above 300 °C. Sample D with 40 nm of a-SiC:H experiences a rapid decline in lifetime immediately following annealing at 300 °C, whereas the passivation of samples containing a-Si only slightly degrades. Above 350 °C, the samples with a-Si:H interface layers experience a sharp decrease in lifetime, while sample C outperforms everything. This discrepancy cannot be fully explained by the difference in diffusion coefficients, as the presence of an a-Si:H top layer leads to drastically different passivating qualities for an a-SiC:H interface layer. Examining the change in hydrogen content within the samples may help illuminate this perceived difference.

4.2 Band gap

The diffusion of hydrogen within the layers is corroborated by the band gap measurements from ellipsometry. Previous studies have established that the typical band gap value for a-Si:H is around 1.7 eV, while a-SiC:H is typically around 2 eV but can exhibit band gaps as wide as 2.3 eV with increased carbon content [30]. As shown in Fig. 6, the band gap of the a-SiC:H interface layer of sample C increases as the temperature approaches 250 °C indicating an increase in hydrogen content within this layer. The band gap of the a-SiC:H layer in sample C remains very constant between 300 and 400 °C , while all other layers exhibit a narrowing band gap in this range. This suggests that the hydrogen content in the a-SiC:H layer of sample C remains consistent at these temperatures, promoting passivation and leading to more steady lifetime measurements relative to other samples.

Fig. 7 provides a graphical representation of the accuracy of the model used to fit the ellipsometric data. As noted, the units of the mean square error is not clearly defined, so the amplitude alone isn't enough to comment on the accuracy of a fit. However, by comparing the changes in MSE between the various device structures we can comment on the relative accuracy of the ellipsometric model for each sample. Below 300 °C, the model is fairly accurate for all samples. However, the accuracy of the fit begins to suffer above this temperature, particularly for samples B and D. This discrepancy is interesting and suggests that the material model used for a-SiC surface layers may be inaccurate after exposure to higher temperatures. In order to comment further on the ellipsometric data, it may be necessary to perform secondary measurements to confirm the accuracy of the models involved.

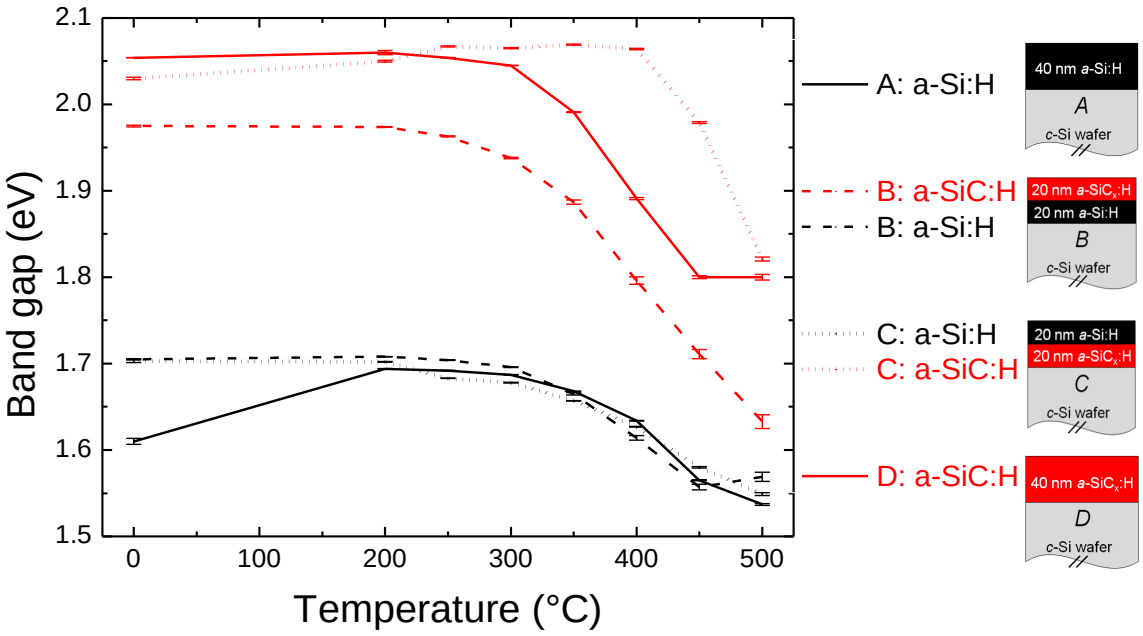

Figure 6. A plot of the optical band gap of the sample layers as a function of annealing temperature

Note: The bars denote an estimation of error for the parameter as provided by the ellipsometric model.

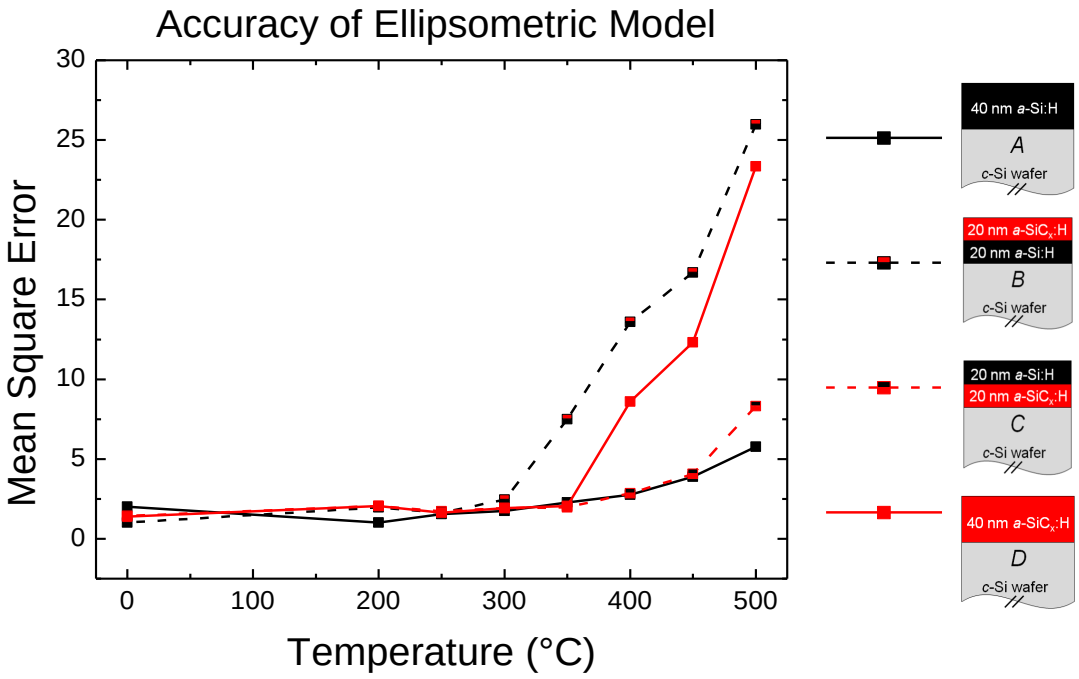

Figure 7. A plot of the mean square error between the curves provide by the ellipsometric model and the experimental data

Note: The units of MSE are not clearly defined, as the model is fitting two different curves with distinct parameters at the same time. Ψ is dimensionless, as it is a ratio of amplitudes, while Δ is an angular phase shift.

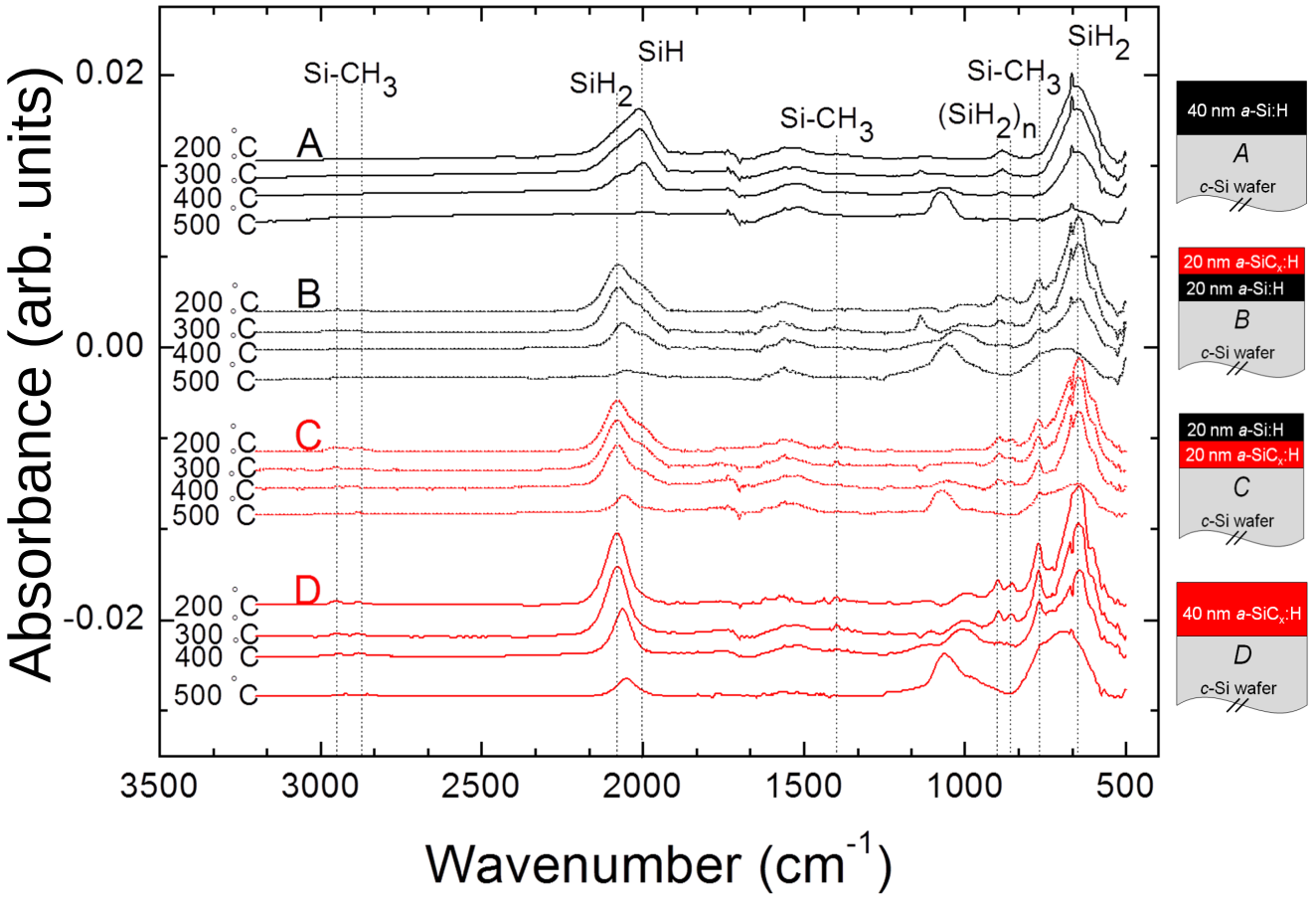

Figure 8. A graph detailing the collected spectra for all experimental samples following annealing

Note: Spectra are shifted along the vertical axis to enable easy comparison. The vertical lines denote spectral peaks of relevant bonding configurations.

4.3 FTIR Spectroscopy

The use of FTIR spectroscopy allows for the identification of bonding structures within the sample layers, independent of the substrate. The unique spectra enables the qualitative comparison of the chemical composition of the samples. By analyzing the spectra, we can make quantitative statements about the concentration of specific bond types, and the concentration of the elements involved. Hydrogen bonding is a major component of surface passivation, so this section will concentrate on silicon-hydrogen bonds in the samples. Hereafter, Si-H will denote silicon-hydrogen bonds in any SiH_n grouping, whereas specific configurations will be represented by SiH, SiH_2, etc.

The low and high stretching modes for Si-H bonds in a-Si:H and a-SiC:H exhibit vibrational frequencies around 2000 and 2080 cm^{-1} respectively [29, 28]. The exact bonding configurations that create these modes is a source of some controversy. It is widely accepted that the low stretching mode (LSM) is attributed to monohydrides, though the exact SiH configurations that contribute is still under discussion [31]. The nature of the high stretching mode (HSM) for Si-H in a-SiC_x:H films is more contentious. Some assign the HSM to dihydrides (SiH_2) [32] while others assign it to monohydride groups incorporated at internal void surfaces [33]. In fact, parsing the distinction between modes due to number of hydrogen bonds versus those related to internal bonding structure is difficult as higher resolutions show a monohydride stretching mode at 2095 cm^{-1} and Si-H_2 stretching modes at 2099 and 2087 cm^{-1} [34]. While the HSM may not exclusively belong per se to a dihydride group, for the purpose of this analysis the LSM peak around 2000 cm^{-1} is assigned to SiH bonds while the HSM peak around 2080 cm^{-1} is assigned to SiH_2.

Incorporating carbon into the films yields unique characteristics, especially after

annealing. A spectral peak around 800 cm^{-1} appears for films which incorporate carbon, as it is linked to the vibrational stretch frequency of Si-CH_3. As demonstrated in Fig. 8 and other studies, samples containing a-SiC:H exhibit a shift of the Si-H HSM peak from 2080 to 2060 cm^{-1} after exposure to temperatures greater than 300 °C [28]. The disappearance of the peaks around 900 and 860 cm^{-1}, related to the bending modes of $(Si\text{-}H_2)_n$ polysilane chains, suggests that the shifted peak at 2060 cm^{-1} is not due to Si-H_2 as commonly believed but rather due to SiH in a cluster environment [34]. This supports the assumption that the peak at 2000 cm^{-1} is indeed a stretching mode of an isolated SiH bond. The lack of LSM peak emergence after annealing suggests that a majority of Si-H_2 is located in clustered form within the a-SiC:H lattice, as the monohydrides formed when hydrogen leaves the SiH_2 groups exclusively exhibit the characteristic stretching mode at 2060 cm^{-1}. It is interesting to note that the sample composed entirely of a-SiC:H only displayed a single spectral peak in the Si-H stretching mode region, centered around the HSM. This bolsters the argument that the Si-H bonds in a-SiC:H are mostly dihydrides in a cluster or monohydrides at internal void surfaces.

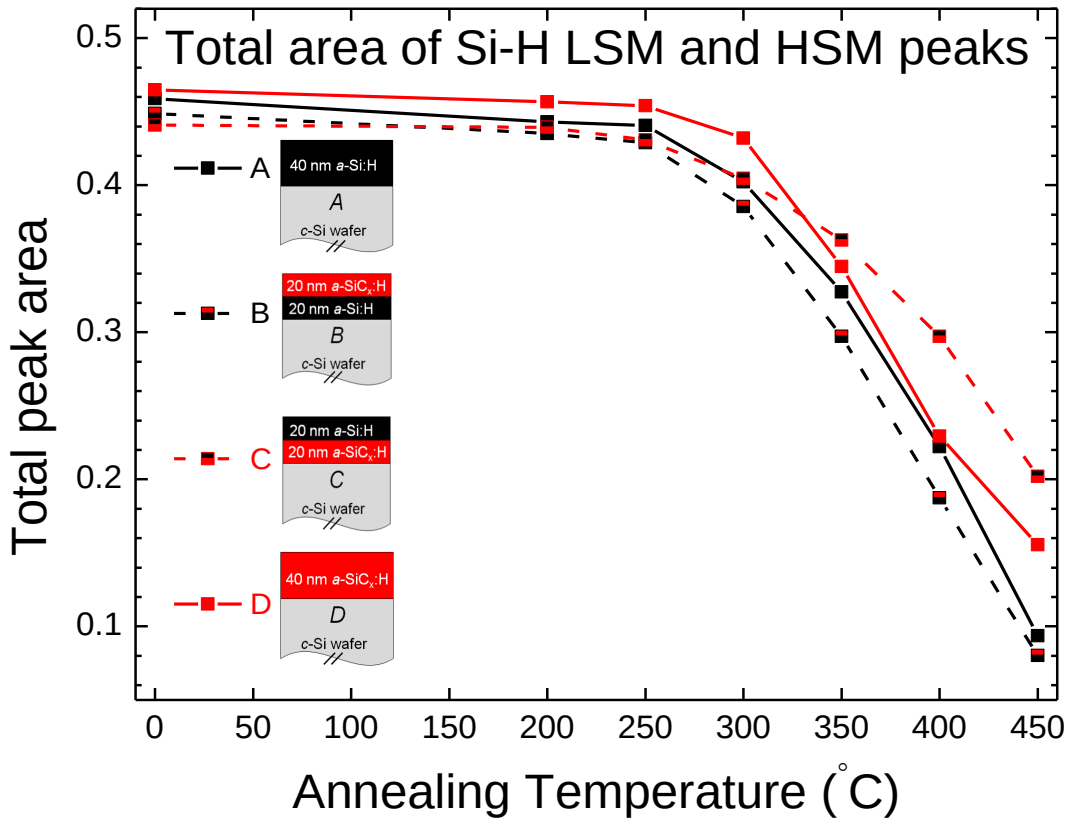

Figure 9. A plot of the total area of the curves fitting the FTIR peaks related to Si-H low and high stretching modes in a-SiC_x:H

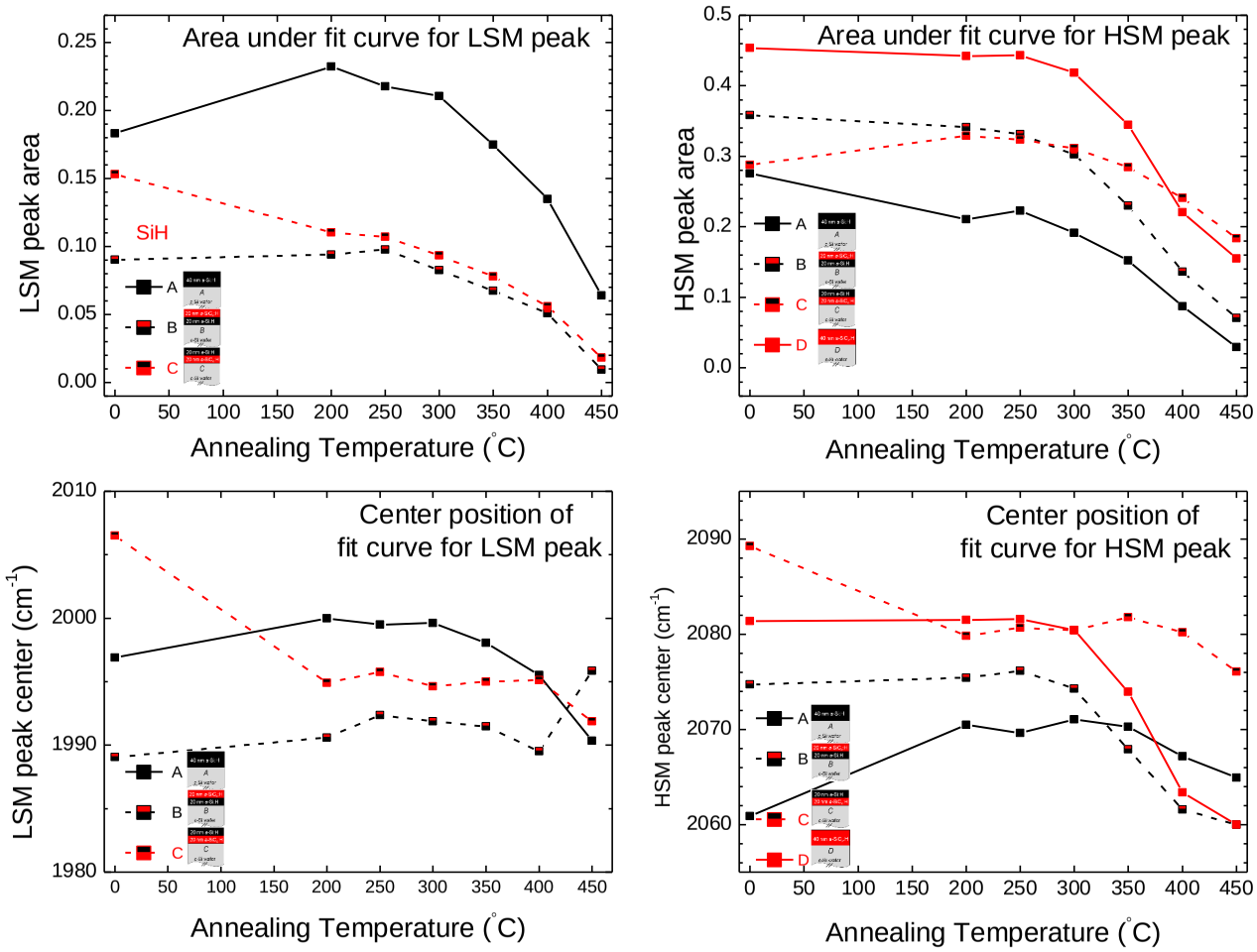

Figure 10. Plots of the position and area of the fitted curves for the Si-H LSM and HSM FTIR peaks

Note: The LSM peak for the 40 nm a-SiC:H layer (sample D) was non-existent so the data has been omitted.

As previously discussed, the area under the curves are related to the concentration of the specific chemical compound that is responsible for the peak. By comparing the fitting curve areas for the Si-H stretching modes, we can draw conclusions about the relative concentration of Si-H bonds within the sample. Fig. 9 displays the total area under the curves used to fit the Si-H LSM and HSM peaks. At high temperatures, sample C containing an a-SiC:H interface layer underneath an a-Si:H "capping" layer exhibits the largest total area. The mechanism behind this phenomenon might be explained by the presence of the a-Si:H "capping" layer. This layer could act as a source for hydrogen for the interface layer, as the lower diffusion coefficient would enable the movement of hydrogen at lower temperatures. At higher temperatures, the hydrogen in the a-SiC:H layer are more tightly bonded and are less apt to diffuse away from interface. It may also be that the top a-Si:H layer acts as a buffer at higher temperatures, preventing the effusion of hydrogen from the sample. The discrepancy in the area of Si-H peaks corresponds exactly with the lifetime measurements, where sample C outperformed the others at temperatures of 350 °C or greater. Another interesting quality of the spectra from sample C is position of the HSM peak, as displayed in Fig. 10. While all other samples containing a-SiC:H display the characteristic shift of the HSM peak towards 2060 cm^{-1} at higher temperatures, the location of HSM peak for sample C stays near 2080 cm^{-1}. This may suggest that the dihydride bonds in sample C are relatively isolated, as the monohydrides left after exposure to high temperatures do not exhibit the characteristic spectral peak of SiH in a cluster group. Coupled with the area calculations and the lifetime measurements, the position of the HSM peak for sample C suggests that non-clustered Si-H bonds tend to withstand high temperatures and lead to better passivation.

4.4 Conclusion

The results of this study confirm the findings by Boccard and Holman, while offering potential explanations for the discrepancy in passivating qualities of a-Si:H and a-SiC:H following high temperature annealing. The sample with an a-SiC:H interface layer and an a-Si:H top layer exhibited the best lifetimes following annealing above temperatures of 300 °C or greater. The ellipsometric band gap results and Si-H peaks in the FTIR spectra suggest that the greater passivation quality is due to increased hydrogen content within the interface layer, specifically bonded in non-cluster configurations. The passivation provided by an a-SiC:H interface layer improves after annealing, surpassing that achieved by a-Si:H. Previous studies by Boccard and Holman corroborate this finding and demonstrate that the passivation achieved by device-relevant stacks containing an intrinsic a-SiC:H layer and a p-type a-Si:H layer is more resilient to high temperatures than that of equivalent stacks of a-Si:H [17]. Furthermore, such stacks were found to have improved transparency, further supporting the utility of intrinsic a-SiC:H and p-type a-Si:H layers as the front stack of an HIT cell. The layers deposited for this study are much thicker than those typically used in an HIT structure, so it may be prudent to extend this analysis to much thinner samples. While thinner stacks would allow for more rapid hydrogen effusion and thus lower lifetimes than thicker stacks, the exhibited relation of lifetime to the carbon content of the passivating layer and silicon bonding configuration suggests a thin layer of a-SiC:H will still exhibit better passivation at high temperatures than an equivalent a-Si:H layer.

Diffuse reflection FTIR spectroscopy was verified as a viable technique for determining the chemical composition of amorphous layers on a polished c-Si substrate, and

the aforementioned process could be easily with an IR transparent window to observe samples in a vacuum environment. These techniques and results set the framework for future experiments to investigate the nature of the silicon-hydrogen bonds and the temperature at which the bonds form and break.

Future work to expound the results of this study and investigate more HIT device-relevant structures could be divided into several steps:

- Utilize the heating and vacuum capabilities of "Anny" the analysis chamber in the Holman Lab in conjunction with a residual gas analyzer (RGA) to obtain effusion data on the previously fabricated samples for this study. Mass spectrometry data using the RGA would illuminate the temperatures at which compounds leave the sample.
- Perform FTIR spectroscopy through an IR transparent window using the diffuse reflection attachment. Heating the sample in "Anny" and obtaining the FTIR spectra will enable direct monitoring of the thermal affects on the sample's chemical bonding configurations with higher temperature resolution than previously reported. Concurrent RGA data would help illuminate the temperatures at which hydrogen effusion overwhelms the diffusion of hydrogen to form new bonds.
- Fabricate HIT structures using textured, p-type c-Si wafers, thin intrinsic, amorphous passivating layer and an n-type amorphous top layer. Repeat the previously discussed techniques to observe the affects doping has on passivation and hydrogen bonding configurations.

REFERENCES

[1] S. D. Wolf, A. Descoeudres, Z. C. Holman, and C. Ballif, "High-efficiency silicon heterojunction solar cells: A review," *Green*, vol. 2, pp. 7–24, 2012.

[2] M. Taguchi, M. Tanaka, T. Matsuyama, T. Matsuoka, S. Tsuda, Y. K. S. Nakano, and Y. Kuwano, "Improvement of the conversion efficiency of polycrystalline silicon thin film solar cell," *Proc. Int. Photovoltaic Sci. Eng. Conf.-5 Tech. Dig.*, pp. 689–692, 1990.

[3] J. I. Pankove and M. L. Tarng, "Amorphous silicon as a passivant for crystalline silicon," *Appl. Phys. Lett.*, vol. 34, no. 156, 1979.

[4] M. Taguchi, A. Terakawa, E. Maruyama, and M. Tanaka, "Obtaining a higher voc in hit cells," *Prog. Photovoltaics*, vol. 13, no. 481, 2005.

[5] M. Taguchi, A. Yano, S. Tohodo, K. Matsuya, Y. Nakamura, T. Nishiwaki, K. Fujita, and E. Maruyama, "24.7% record efficiency hit solar cell on thin silicon wafer," *IEEE J. Photovoltaics*, vol. 4, no. 1, pp. 96–99, Jan. 2014.

[6] Z. C. Holman, A. Descoeudres, L. Barraud, F. Z. Fernandez, S. D. W. J. P. Seif, and C. Ballif, "Current losses at the front of silicon heterojunction solar cells," *IEEE J. Photovoltaics*, vol. 2, no. 7, 2012.

[7] S. D. Wolf and M. Kondo, "Nature of doped a-si:h/c-si interface recombination," *J. Appl. Phys*, vol. 105, no. 103707, 2009.

[8] K. N. Yaung, J. R. Lang, and M. L. Lee, "Towards high efficiency gaasp solar cells on (001) gap/si," in *2014 IEEE 40th Photovoltaic Specialist Conference (PVSC)*, IEEE, 2014, pp. 0831–0835.

[9] R. Petres, I. Martin, M. Vetter, D. Baetzner, J. Tan, A. Cuevas, and R. Alcubilla, "Surface and emitter passivation of crystalline silicon by amorphous silicon carbide: Evolution with annealing," in *21st EU PVSEC*, 2006, pp. 919–922.

[10] W. Beyer and H. Mell, "Disordered semiconductors," in, M. A. Kastner, G. A. Thomas, and S. R. Ochinsky, Eds. Plenum Press, 1987, ch. Composition and Thermal Stability of Glow-Discharge a-Si:C:H and a-Si:N:H Alloys, pp. 641–658.

[11] R. Ferre, I. Martın, P. Ortega, M. Vetter, I. Torres, and R. Alcubilla, "N - type emitter surface passivation in c - si solar cells by means of antireflective amorphous silicon carbide layers," *J. Appl. Phys*, vol. 100, no. 073703, 2006.

[12] S. Janz, S. Riepe, M. Hofmann, S. Reber, and S. Glunz, "Phosphorus-doped sic as an excellent p-type si surface passivation layer," *Appl. Phys. Lett.*, vol. 88, no. 133516, Mar. 2006.

[13] C. Ehling, D. Treptow, G. Bilger, F. Einsele, and M. B. Schubert, "Electronic surface passivation of crystalline silicon solar cells by a-sic:h," *IEEE*, pp. 1368–73, 2010.

[14] A. Gaugrès, F. Husser, E. Fourmond, and M. Lemiti, "Passivating properties of hydrogenated amorphous silicon carbide deposited by pecvd technique for photovoltaic applications," *Energy Procedia*, vol. 38, no. 823, 2013.

[15] A. Descoeudres, Z. C. Holman, L. Barraud, S. Morel, S. D. Wolf, and C. Ballif, "21% efficient silicon heterojunction solar cells on n- and p-type wafers compared," *IEEE J. Photovoltaics*, vol. 3, no. 1, pp. 83–89, 2013.

[16] D. Pysch, M. Bivour, M. Hermle, and S. W. Glunz, "Amorphous silicon carbide heterojunction solar cells on p-type substrates," *Thin Solid Films*, vol. 519, pp. 2550–2554, 2011.

[17] M. Boccard and Z. C. Holman, "Amorphous silicon carbide passivating layers for crystalline-silicon-based heterojunction solar cells," *J. Appl. Phys*, vol. 118, no. 065704, 2015.

[18] D. K. Schroder, *Semiconductor Material and Device Characterization*. New York: Wiley, 1990.

[19] E. Yablonovitch and T. J. Gmitter, "A contactless minority carrier lifetime probe of heterostructures, surfaces, interfaces and bulk wafers," *Solid-State Electorn.*, vol. 35, pp. 261–267, Mar. 1992.

[20] T. Hama, H. Okamoto, Y. Hamakawa, and T. Matsubara, "Hydrogen content dependence fo the optical enegry gap in a-si:h," *J. Non-Cryst. Solids*, no. 59, pp. 333–6, 1983.

[21] T. F. Schulze, L. Korte, F. Ruske, and B. Rech, "Band lineup in amorphous/crystalline silicon heterojunctions and the impact of hydrogen microstructure and topological disorder," *Phys. Rev. B*, vol. 83, no. 165414, Apr. 2011.

[22] M. A. Petrich, K. K. Gleason, and J. A. Reimer, "Structure and properties of amorphous hydrogenated silicon carbide," *Phys. Rev. B*, vol. 36, no. 18, pp. 9722–31, Jun. 1987.

[23] P. F. Kane and G. B. Larrabee, *Characterization of Semiconductor Materials*. McGraw-Hill, 1970.

[24] H. G. Tompkins and W. A. McGahan, *Spectroscopic Ellipsometry and Reflectometry*. John Wiley & Sons, 1999.

[25] G. E. J. Jr. and F. A. Modine, "Parameterization of the optical functions of amorphous materials in the interband region," *Appl. Phys. Lett.*, vol. 69, no. 3, p. 371, Jul. 1996.

[26] J. Budai, I. Hanyecz, E. Szilágyi, and Z. Tóth, "Ellipsometric study of sixc films: Analysis of tauc–lorentz and gaussian oscillator models," *Thin Solid Films*, vol. 519, no. 9, pp. 2985–2988, 2011.

[27] P. R. Griffiths and J. A. de Haseth, *Fourier Transform Infrared Spectrometry*, 2nd. New Jersey: John Wiley & Sons, 2007.

[28] W.-L. Lin, H.-K. Tsai, S.-C. Lee, W.-J. Sah, and W.-J. Tzeng, "Identication of infrared absorption peaks of amorphous silicon-carbon alloy by thermal annealing," *Appl. Phys. Lett.*, vol. 51, no. 25, pp. 2112–4, Oct. 1987.

[29] M. H. Brodsky, M. Cardona, and J. J. Cuomo, "Infrared and raman spectra of the silicon-hydrogen bonds in amorphous silicon prepared by glow discharge and sputtering," *Phys. Rev. B*, vol. 16, no. 8, pp. 3556–71, Oct. 1977.

[30] J. M. Essick, Z. Nobel, Y.-M. Li, and M. S. Bennett, "Conduction- and valence-band offsets at the hydrogenated amorphous silicon-carbon/crystalline silicon interface via capacitance techniques," *Phys. Rev. B*, vol. 54, p. 4885, Aug. 1996.

[31] A. H. M. Smets, W. M. M. Kessels, and M. C. M. van de Sanden, "Vacancies and voids in hydrogenated amorphous silicon," *Appl. Phys. Lett.*, vol. 82, no. 10, pp. 1547–9, Jan. 2003.

[32] G. Lucovsky, R. J. Nemanich, and J. C. Knights, "Structural interpretation of the vibrational spectra of a-si: H alloys," *Phys. Rev. B*, vol. 19, no. 2064, 1979.

[33] W. Beyer and M. S. A. Ghazala, "Absorption strengths of si-h vibrational modes in hydrogenated silicon," *Res. Soc. Symp. Proc.*, vol. 507, no. 601, 1998.

[34] H. Wagner and W. Beyer, "Reinterpretation of the silicon-hydrogen stretch frequencies in amorphous silicon," *Solid State Commun.*, vol. 48, no. 7, pp. 585–587, 1983.

[35] S. Kaplan, F. Jansen, and M. Machonkin, "Characterization of amorphous carbonhydrogen films by solidstate nuclear magnetic resonance," *Appl. Phys. Lett.*, vol. 47, no. 7, pp. 750–9, Oct. 1985.

[36] F. Demichelis, C. F. Pirri, and E. Tresso, "Influence of doping on the structural and optoelectronic properties of amorphous and microcrystalline silicon carbide," *J. Appl. Phys*, vol. 72, pp. 1327–33, Apr. 1992.

[37] D. A. Anderson and W. E. Spear, "Electrical and optical properties of amorphous silicon carbide, silicon nitride and germanium carbide prepared by the glow discharge technique," *Philosophical Magazine*, vol. 35, pp. 1–16, 1977.

[38] R. A. Sinton and A. Cuevas, "Contactless determination of current–voltage characteristics and minority carrier lifetimes in semiconductors from quasisteadystate photoconductance data," *Appl. Phys. Lett.*, vol. 69, no. 17, pp. 2510–2, Oct. 1996.

[39] S. King, M. French, K. Bielefeld, and W. Lanford, "Fourier transform infrared spectroscopy investigation of chemical bonding in low-k a-sic:h thin films," *J. Non-Cryst. Solids*, vol. 357, pp. 2970–83, Apr. 2011.

[40] A. H. M. Smets, T. Matsui, and M. Kondo, "Infrared analysis of the bulk silicon-hydrogen bonds as an optimization tool for high-rate deposition of microcrystalline silicon solar cells," *Appl. Phys. Lett.*, vol. 92, no. 033506, pp. 1–3, Jan. 2008.

[41] H.-K. Tsai, W.-L. Lin, W.-J. Sah, and S.-C. Lee, "The characteristics of amorphous silicon carbide hydrogen alloy," *J. Appl. Phys*, vol. 64, no. 4, pp. 1910–5, Apr. 1988.

[42] A. H. M. Smets and M. C. M. van de Sanden, "Relation of the si-h stretching frequency to the nanostructural si-h bulk environment," *Physical Review B*, vol. 76, no. 073202, pp. 1–4, Aug. 2007.

[43] S.-Y. Lin and S. Chang, "Variations of vibrational local modes and electronic states of hydrogenated amrphous silicon carbide under thermal annealing," *J. Phys. Chem. Solids*, vol. 59, no. 9, pp. 1399–1405, Jun. 1998.

[44] C. Manfredotti, F. Fizzotti, M. Boero, P. Pastorino, P. Polesello, and E. Vittone, "Influence of hydrogen-bonding configurations on the physical properties of hydrogenated amorphous silicon," *Phys. Rev. B*, vol. 50, no. 24, pp. 18 046–53, Dec. 1994.